NUMERICAL INVESTIGATIONS ON SMALL-SCALE ROTOR CONFIGURATIONS WITH VALIDATION USING ACOUSTIC WIND TUNNEL DATA

Jianping Yin, Jianping.Yin@dlr.de, DLR, AS-HEL (Germany)
Karl-Stephane Rossignol, Karl-Stephane.Rossignol@dlr.de, DLR, AS-TEA (Germany)
Lukas Rottmann, Lukas.Rottmann@dlr.de, DLR, AS-HEL (Germany)
Thorsten Schwarz, Thorsten.Schwarz@dlr.de, DLR, AS-HEL (Germany)

ABSTRACT

This paper addresses the acoustic and aerodynamic characteristics of small-scale rotor configurations, including the influence of the rotor-rotor interactions. For this purpose, a Rotor/Rotor/Pylon configuration is chosen for both the test and numerical simulations. The wind tunnel experiments on various rotor configuration were performed in DLR's Acoustic Wind Tunnel Braunschweig (AWB). The experiments involve isolated rotors, and rotors in tandem and coaxial configuration in hover and forward flight. For numerical simulations an unsteady free wake 3-D panel method (UPM) is used to account for aerodynamic non-linear effects associated with the mutual interference among the Rotor/Rotor/Pylon configurations. The effect of the pylon is simulated using potential theory in form of a panelized body. Finally, the sound propagation into the far field is calculated with DLR's FW-H code APSIM, using UPM blade surface pressure as input. The validation effort is supported by CFD TAU steady simulations on selected hover test cases. The experiments and numerical results indicate that the harmonic noise is the dominant source of the noise for the present rotor selection. Broadband noise is also observed in the experiment, but its contribution to the overall sound pressure is small. In the numerical simulations of both the coaxial and the tandem configuration, the interferences are particularly well visible and the noise directivity becomes more complex. There is no change in time averaged inflow by applying phase angles. In the coaxial condition, in hover, the phase delay between rotors doesn't change the maximum noise level. In forward flight, the phase delay can influence the maximum level of the noise radiation. In both coaxial and tandem configuration, the position of the downstream rotor is key for the noise radiation and therefore avoiding the interaction with upstream wake can reduce the noise radiation.

ABBREVIATIONS

UPM	Unsteady Panel Method
APSIM	DLR FW-H code
TAU	DLR unstructured computational fluid dynamics code
FW-H	Ffowcs-Williams/Hawkings acoustic analogy
rev	Revolution
V_∞	Flight speed, m/s
D	Rotor diameter (0.33m)
RHR	Right Handed Rotor
LHR	Left Handed Rotor
RPM	Rotor rotations per minute
BPF	Blade Passing Frequency, Hz
SPL	Sound Pressure Level, dB
OASPL	Overall Sound Pressure Level, dB
T	Thrust in N
M_h	Hover tip Mach number
Φ	Azimuth angle, deg
θ	Polar angle, deg
$C_N M^2$	Normal force coefficient
p_0	Air pressure in undisturbed medium, pa

1. INTRODUCTION

In the context of a growing interest in developing Urban Air Mobility (UAM) solutions to congestion problems in urban traffic, there is a need to provide answers to fundamental questions about the aerodynamic and acoustic properties of these new vehicles [1][2]. Urban Air Mobility Vehicles (UAMVs) usually refers to small aircraft capable of transporting one to five passengers for intercity transportation. Multirotor systems are popular for UAM. Usually open rotors are selected which are significant sources of tonal and broadband noise. Due to their smaller scales, compared to helicopter rotors or aircraft propellers, broadband noise components may have a greater importance in the overall sound emission as blade tip Mach numbers are relatively low and blade loading is lower. Thus, tonal source components are expected to be dominant only for the first few harmonics. In order to be publicly accepted, the noise of Urban Air Vehicles must be barely audible compared to the city's background noise. Therefore, Urban Air Vehicles must be designed from the beginning to meet stringent noise standards. To gain valuable insights into these issues, numerical tools to predict noise emissions from small rotors in both isolated and compound configurations are required.

This paper will focus on the results from numerical activities for the small rotor configurations, especially rotor/rotor configurations and their comparisons with selected wind tunnel test data. For this purpose, the experimental approach used to obtain data will be first presented. The methodologies applied in the numerical simulations will then be described. The acoustic predictions for various rotor configurations

as shown in Figure 1 will be analysed and validated with available experimental and CFD results. The analysis also includes the different sources of noise in the test data. The acoustic results will be presented in terms of the overall sound pressure level (OASPL) directivities and the spectrum.

Figure 1 Experimental setup: single rotor (left), coaxial rotors (middle) and tandem rotors (right)

2. DESCRIPTION OF WIND TUNNEL MODEL AND TEST

Validation cases for the prediction of noise emissions of the small rotors are taken from DLR AACID (Acoustics and Aerodynamics for CIty Drones) wind tunnel tests carried out in 2021. Completed AWB (Acoustic Wind Tunnel Braunschweig) measurement for several propeller configurations include isolated, coaxial, tandem with vertical and lateral offset as shown in Figure 1 and Figure 2.

2.1 Test setup

The AWB[3] is DLR's small-scale high-quality anechoic testing facility. It is an open-jet Göttingen-type wind tunnel capable of running at speeds of up to 65 m/s and optimized for noise measurements at frequencies above 250 Hz. The nozzle is 1.2 m high by 0.8 m in width. A special rig was designed to extend the capabilities of the facility to meet the requirements of simultaneous measurements of multiple rotors under static and flight conditions, e.g. Figure 1 and Figure 2.

The main objective of the selected mechanical design is to enable the investigation of the effect of flow and shaft angle on the acoustic radiation of a broad range of propeller configurations; isolated, coaxial, tandem with vertical and lateral offset, e.g. Figure 1. The dimensions of the AWB test section, allow the investigations of rotors with a diameter of up to approximately 0.4 m. The rig is designed to allow shaft angle variations in the range $\alpha \pm 30°$ and testing at free-stream velocities up to $U_\infty \approx 30\ \mathrm{m/s}$.

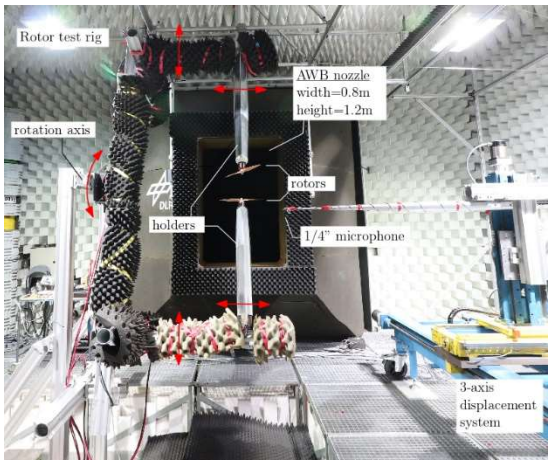

Figure 2 Overview of the full test rig and microphone setup installed in the AWB's test section. Center: coaxial configuration

Above $U_\infty \approx 30\ \mathrm{m/s}$, rig vibrations will have a noticeable influence on the loads, moments and acoustic measurements. Furthermore, the rig allows for lateral spacing settings in the range $\Delta y \pm 0.15\ \mathrm{m}$, streamwise spacing settings in the range $\Delta x \pm 0.3\ \mathrm{m}$ and vertical spacing settings in the range $\Delta z \pm 0.3\ \mathrm{m}$. These setting values are evidently valid for the current set of propellers considered herein. The whole structure of the rig is based on standard X-95 rails and carriers. This choice allows for easy changes in configuration. The rig is fixed to a rotating axle at its center point, i.e. on the left-hand side of Figure 2 to allow variations in rotor shaft angle.

2.2 Rotor and support (pylon) model

Several sets of the rotor are tested. For current paper, the test results from a two blade 13x7 rotor are chosen for comparing with the numerical simulation. The rotor 13x7 represents a rotor with 13 inch or 0.33m in diameter and 7 inch in pitch, as shown in Figure 3. The rotor pitch is defined here as the distance the rotor would move forward in one rotation if it were moving through a soft solid. The rotor is a commercially available one. A close inspection shows that the two rotor blades have a slightly different shape.

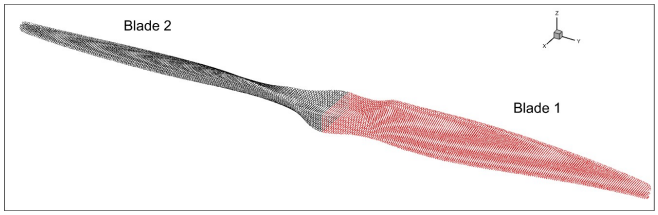

Figure 3 rotor 13x7 geometry (in right handed rotor (RHR) configuration

The rotors are propelled by Leopard LC5065 motors coupled to YGE 205HVT speed controllers and

SM300-Series 3300 W DC power supplies. This combination allows RPM up to 13000 to be reached. For each rotor, performance data, in terms of thrust and torque, is acquired through miniature six-components load cells, Modell K6D40 from ME-Meßsysteme GmbH, mounted directly underneath the propellers. Each rotor RPM is acquired through a 1/rev signal generated by a Hall-effect sensor mounted to the rotor's shaft. This signal also serves as a trigger signal for data post-processing. The flight conditions include hover, climb and approach for different flight speeds

2.3 Aerodynamic and acoustic measurement

For each rotor, performance data, in terms of thrust and torque, is acquired through miniature six-components load cells, Model K6D40 from ME-Meßsysteme GmbH Germany, mounted beneath the motors. The load cells are separated from the motors by an aluminum block spacer to reduce as much as possible the influence of temperature variations and that of the motor's electromagnetic field on the measurements.

The load cells are strain-gauge-based instruments which measure three orthogonal forces $(\mathrm{F_x}, \mathrm{F_y}, \mathrm{F_z})$ and three orthogonal moments $(\mathrm{M_x}, \mathrm{M_y}, \mathrm{M_z})$. The load cells were factory calibrated by the manufacturer to a full-scale thrust $F_z = 200\ \mathrm{N}$ $(\mathrm{F_x} = \mathrm{F_y} = 50\ \mathrm{N})$ and a full-scale torque $\mathrm{M_z}$ of $5\ \mathrm{Nm}$. The load cell signals are sampled at a rate of 5 Hz by the manufacturer-provided pre-conditioning amplifier box. The manufacturer's data sheet rates the load cell with a precision of 0.2% full-scale, corresponding to 0.4 N. Preliminary investigations have shown that this value is strongly dependent on temperature variations and is also RPM dependent, i.e. load dependent. A conservative estimate of the bias error on the load measurement is 0.5% full-scale, though in the experiment this error was minimized through frequent zeroing of the load cells and short measurement time. The precision of the load cells is within the range given by the manufacturer (i.e. 0.2% full-scale).

The rotor's acoustic emission was acquired through a single 1/4" Brüel und Kjær 4136 pressure field microphone mounted to a 3-axis linear displacement system e.g. Figure 2. The microphone was placed in the flow field with its membrane protected by a Brüel und Kjær nose cap. The microphone was aligned parallel to the flow field with its sensing surface pointing upstream. The selected measurement positions are depicted in Figure 10.

The acoustic signal, along with the 1/rev signal, are sampled at a 100 kHz rate on a GMB Viper GmbH 48 channel data acquisition unit. A high-pass digital filter is used to remove low frequency noise contamination due to the wind tunnel flow. The filter characteristic is removed in the data processing steps. The processing takes advantage of the 1/rev signal to phase-lock the data on a revolution per revolution basis prior to spectral and time domain analysis. Each data block is normalized to a unit revolution time to account for fluctuations in total revolution sample count. The typical standard deviation of the sample count per revolution is on the order of 1 to 2 samples, i.e. $10\ \mu s$ to $20\ \mu s$, depending on the configuration and RPM, with lower RPM showing smaller variations. Prior to Fourier analysis, 32 individual blocks, i.e. revolutions, are stacked together to form a sufficiently long time series to achieve a high frequency domain resolution. Each time series is then Fourier transformed using a Hanning window to minimize spectral leakage issues. Averaged spectra are obtained through ensemble averaging of individual spectra and through time domain ensemble averaging prior to the Fourier analysis step. Spectral averaging preserves the broadband content of the signals, whereas time domain averaging tends to reduce it due to its incoherent nature and thus emphasize the harmonic components. Further details about the aerodynamic measurements, signal to noise ratio considerations as well as an evaluation of the useful frequency range are provided in [4].

3. DESCRIPTION OF METHODOLOGIES APPLIED IN NUMERICAL SIMULATIONS

The aeroacoustic computation into the far field is split into two steps: In a first step the aerodynamic pressure data on the source surface or perturbation nearfield around the source surface is computed by either high or mid fidelity aerodynamic tools; in a second step the sound propagation into the far field is calculated with an acoustic code using aerodynamic input.

3.1 Mid fidelity aerodynamic tool, UPM

UPM[5][6][7][8][9] is a velocity-based, indirect potential formulation – a combination of source and dipole distribution on the solid surfaces on the rotor or wing surface and dipole panels in the wake as shown in Figure 4. A short zero-thickness elongation of the trailing edge along its bisector, called Kutta panel, ensures the flow tangency condition at the trailing edge and defines the total strength of the circulation at the blade section. An iterative pressure Kutta condition is implemented to subsequently ensure pressure equality at the trailing edge. This method is proved to be computationally efficient and robust with respect to the size of the chosen time step and the number of panels on the blade.

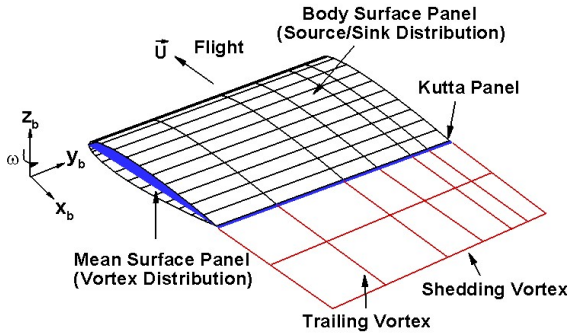

Figure 4 Numerical model of a blade and wake

The pressure on the blade surface is calculated from the unsteady Bernoulli equation. The compressibility effect is only considered in computing the normal force coefficient by applying Prandtl-Glauert correction. The free wake is represented in the form of connected vortex filaments and is released from the downstream edge of the Kutta panel. The spanwise variation of the circulation on the wake panels is the same as that on the Kutta panels and is kept unchanged throughout the whole computations. The wake can also be represented in the form of vortex particles as UPM is linked to a particle solver originally coded for the DUST-panel method [10] by the Politecnico di Milano. The particle wake method promises an improved simulation robustness for cases where straight line vortex filaments would cross solid body surfaces. To accurately predict blade vortex interaction (BVI), especially parallel BVI, a hybrid method combining the wake panel model and particle model can be applied.

It is possible in UPM to activate an approximate boundary layer (BL) analysis [9] for lifting and non-lifting bodies. Various simple integral methods for laminar / turbulent BL analysis are employed for predicting the BL. The laminar and the turbulent separation criteria are part of the integral methods (usually based on shape factor values). The analysis is based on sectional flow properties easily defined thanks to structured panel surfaces in UPM. Instead of defining laminar and the turbulent BL according to the integral methods, the BL transition can also be set at a fixed chordwise position using a tripping marker. If flow separation is predicted, the boundary layer analysis ends immediately at the separation point. The BL analysis is performed as a pure postprocessing step based on the inviscid potential flow solution. The results are not fed back to the potential flow solver to account for the displacement of the outer inviscid flow. Therefore, there is no correction on the blade surface pressure.

3.2 High fidelity aerodynamic tool, CFD TAU

The unstructured CFD code TAU is based on the solution of the Reynolds averaged Navier-Stokes equations on hybrid unstructured meshes. The solver relies on a cell vertex scheme to discretize the mass, momentum and energy fluxes [11]. For the AACID simulations the second order accuracy central scheme was used for spatial discretization. Scalar dissipation has been used as the central dissipation scheme. The temporal discretization is based on an explicit Runge-Kutta scheme. As turbulence model the two-equation turbulence model Menter SST was used. Furthermore, all surfaces were simulated fully turbulent. In order to accelerate the simulation, full multigrid was applied. A convergence of at least six orders of magnitude is ensured for all simulations.

The mesh used for the simulation is built entirely with hexaeder and has a mesh count of 34 millio. mesh points. The entire propeller was meshed including both rotor blades and the connecting hub. 214 mesh points were used in the airfoil circumference and 234 mesh points were used along the span. The far-field is located about 116 rotor diameters from the propeller and is realized from propeller surface to far-field edge with 176 mesh points.

3.3 Vortex core radius and aerodynamic trim computation

For Mid-Fidelity UPM aerodynamic simulations, an inviscid and potential flow is assumed. In UPM, the wake dissipation is realized using a vortex core radius model. Therefore, the choice of a proper vortex core radius as well as a vortex core radius aging model is a key to determine the proper induced inflow velocity for the rotor. For example, a small vortex core radius can increase the inflow downwash velocity and therefore reduce rotor thrust as a consequence of a reduction of the effective blade angle of attack. The rotor thrust for the 13x7 rotor (Figure 3) as function of rotor revolutions for two vortex core radii is given in Figure 5 for RPM 12000. For comparisons both the AWB test data and the time averaged TAU results are also plotted. As expected the thrust level for the large core radius (green dashed line) is higher. In general, the UPM results show a higher thrust level than both the test and CFD TAU results. The TAU simulation shows significant flow separations along the complete span of the blades (Figure 9). These separations are also predicted by UPM's boundary layer code. However, as UPM solves the potential flow, these separations are not included in the flow computation. The reason for the large differences of the TAU thrust to the thrust observed in the experiment is still unclear.

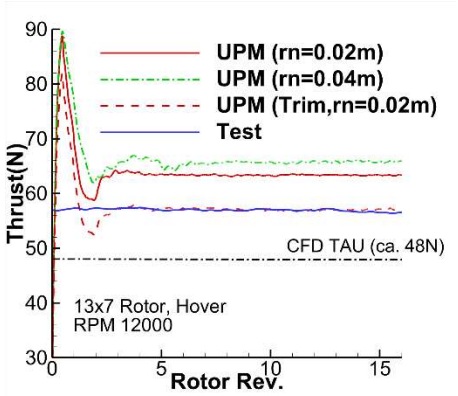

Figure 5 Rotor thrust as a function of rotor revolutions and vortex core radius

In order to have a fair comparison for noise emission between experimental data and numerical simulations, the trim condition between the numeric and experiment should be matched. Therefore, a trim to the measured thrust is applied. Here the flow conditions such as rotor shaft, advance ratio and RPM are fixed. In general, there are two ways which can be used to change simulated thrust value, adjusting vortex core radius as demonstrated in Figure 5 and adjusting blade pitch control angle. Here a fixed vortex core radius as rn=0.02m is used to assure a good stability of the wake development. A force trim according to the rotor thrust from the test is used. The blade pitch control angles are determined by the trim algorithm in such a way that the thrust matches the experimental value in a given tolerance, as shown by the red dashed line in Figure 5. For this trim example, a pitch decrease of about 1.62 deg is required to match the experimental value.

In the rotor/rotor interaction cases, the trim procedure is then applied to both rotors simultaneously to consider the multi-influence of rotors.

3.4 The Aeroacoustic Model

The Aeroacoustic Prediction System based on an Integral Method, APSIM has been developed at the DLR Institute of Aerodynamics and Flow Technologies (DLR AS) for the prediction of rotor or propeller noise radiation in the free field. The method is designed to calculate wave propagation over large distances in uniform flows. The methodology is based on the Ffowcs-Williams/Hawkings (FW-H) formulation for porous and blade surfaces. Only linear sound propagation is considered. In this study, the blade surface pressure data computed by UPM or TAU are used as input for APSIM. The calculations, performed in the time domain, deliver a pressure time history at any desired observer location, which can be Fourier analyzed to derive acoustic spectrum data. APSIM has been extensively applied for the aeroacoustic analysis of a wide range of helicopter and propeller configurations, and in recent times the coupling of the code to the CFD solver TAU has been matured and automated to a great degree.

4. RESULTS FOR THE ISOLATED ROTOR

The rotor 13x7 (Figure 3) is chosen for the UPM simulations. A total of 16 rotor rotations for hover and 6 rotor rotations for forward flight were computed in order to obtain a fully periodic solution. In hover, the wakes are transported only by the induced velocity and, but not by some on-flow velocity. Therefore, a longer computation is required to get rid of the influence from the starting vortices.

The computation proceeded in azimuthal steps of 5° for the hover and 2° for the forward flight. Each blade was discretized in the present study by 49 planar surface elements (panels) along the profile contour and 30 panels along the span. A half-cosine spacing was used along the blade span.

4.1 Hover at RPM= 8000,10000,12000

4.1.1 Trim conditions

The collective pitch correction as well as the achieved rotor thrust are summarized in Table 1 and Figure 6 for different rotor RPM. The pitch angle here represents an addition angle added to the blade. A negative value means a reduction on the pitch angle. The thrust matches the experimental value in a given tolerance within 0.5 N.

Table 1 Trim conditions

V_∞ m/s	RPM	M_h	Pitch UPM	Thrust UPM	Thrust Test
0	8000	0.41	-1.08°	24.4	24.7
0	10000	0.51	-1.11 °	39.6	39.8
0	12000	0.61	-1.62°	57.5	57.2

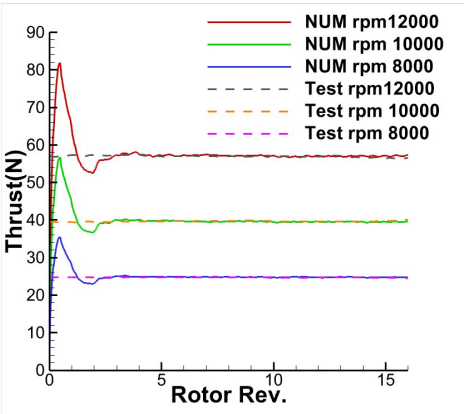

Figure 6 Rotor thrust as function of rotor revolutions

The thrust time history from the UPM simulations shows that with the start of the rotor revolution, the thrust in the simulation increases steeply and then settles down to a fairly constant value after some revolutions. This thrust build up is due to the strong starting vortex which is shed off the blade trailing edge at the impulsive start of the rotor. With the progress of the computation, the starting vortices move away from the blades and the normal wake structure, which is relevant for the practical situation, develops as demonstrated by the fairly constant thrust values.

4.1.2 Aerodynamics

The comparison of the blade surface pressure distribution represented as p-p_0 (unsteady surface pressure) between TAU and UPM is given in Figure 7 and Figure 8 for RPM 12000 and 10000 respectively. The p_0 is air pressure in undisturbed medium. The p-p_0 distribution between TAU and UPM resembles very good correlations in terms of pressure pattern and amplitude in both suction and pressure side. The difference mainly occurs in the trailing edge area, especially towards the blade root region where a large flow separation region is observed in the TAU simulation as shown in Figure 9. However, UPM solves only the potential flow.

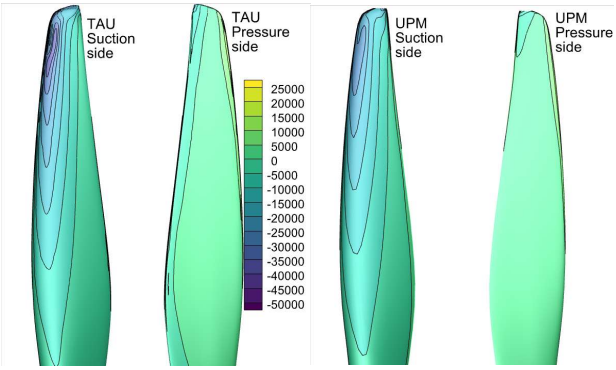

Figure 7 Suction and pressure side distribution of the p-p_0 for TAU and UPM at rpm 12000

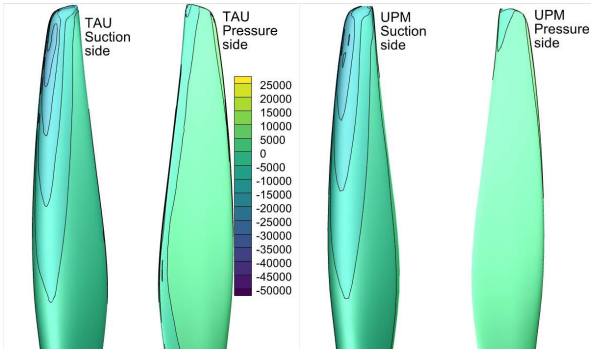

Figure 8 Suction and pressure side distribution of the p-p_0 for TAU and UPM at rpm 10000

Similar characteristics in terms of p-p_0 distribution are also observed for RPM 8000 which are not shown here.

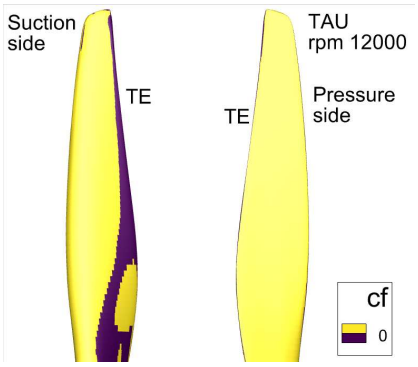

Figure 9 Separation line predicted by CFD TAU for rpm 12000

4.1.3 Acoustics

The FW-H impermeable surface approach uses blade surface data as input. For this approach, only the surface pressure time histories are needed and hence only noise contributed from monopoles and dipoles can be included. In the present study the unsteady pressure data on the rotor blade are used as input to APSIM. The presentation of the acoustic results will focus on data taken in the test on a polar arc represented by microphones from number 5 to 11 in Figure 10. The arc is located in the X-Z plane with the arc radius of 0.3m and polar angle difference of 15°. The microphone 9 is located in the rotational plane (X-Y). Results will be presented in terms of overall sound pressure level (OASPL) directivities and spectrum.

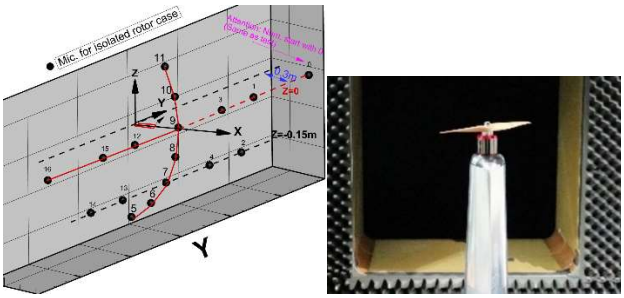

Figure 10 Microphone positions (Left) for the isolated rotor (Right) case.

The polar directivity for the OASPL is shown in Figure 11 for the 13x7 rotor and RPM 12000. Experimental data as well as simulation results from UPM and TAU are presented. In addition, the OASPL obtained from the experiment using two different averaging technique is included. As mentioned in the previous section, the advantage of the time averaged noise spectrum is that the random or stochastic noise, such as broadband noise or flow noise with non-periodicity behavior can be removed or reduced dramatically.

Therefore, the difference between spectrum averaging method and time averaging method can provide an estimated of the non-harmonic source contribution.

In general, the contribution of the broadband noise to the OASPL is negligible in the measurement results for all the microphones except microphone five. For microphone 5 at RPM 12000 the OASPL (black open square) computed using spectral averaging is significantly higher than the OASPL (blue solid circle) computed with time averaging. This is because the microphone five is located directly below the rotor and the rotor downwash increases the microphone self-noise. By reducing the rotational speed, the strength of the rotor downwash is reduced and the microphone self-noise is reduced too. Therefore, the difference between the two averaged data is reduced.

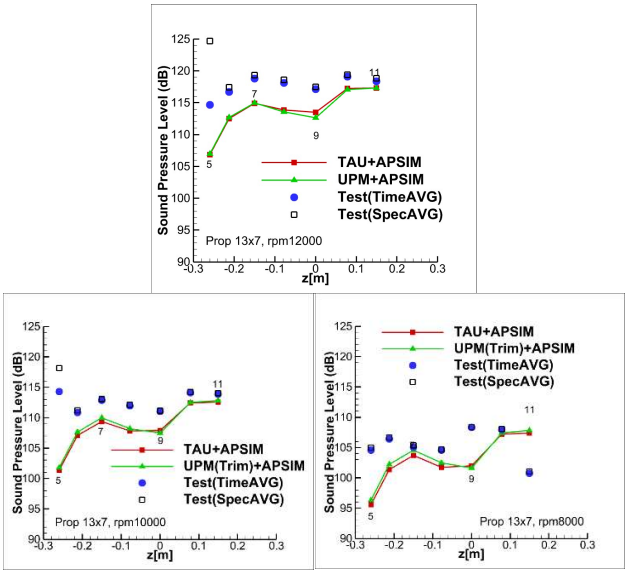

Figure 11 Polar directivity for OASPL at polar microphone from 5 to 11. Comparison of predictions with measurements [4]

The results of Figure 11 indicate that the trimming procedure allows the UPM simulations match TAU results. The acoustic simulations are able to capture the experimental trends, especially for the microphone located above the rotor rotational plane. There are in general higher OASPL levels in the measurements for the microphone below the rotational plane, where acoustic scattering of the pylon support may play a role, which were not included in the acoustic simulations.

Figure 12 and Figure 13 present the acoustic spectrum for the microphone located at positions 8, 9 and 10. The frequency range of the spectrum is limited to 6 kHz for clearness purposes. The useful frequency range of the experimental data exceeds 20 kHz. It should be mentioned that broadband sound and motor noise contributions were not included in the numerical simulation.

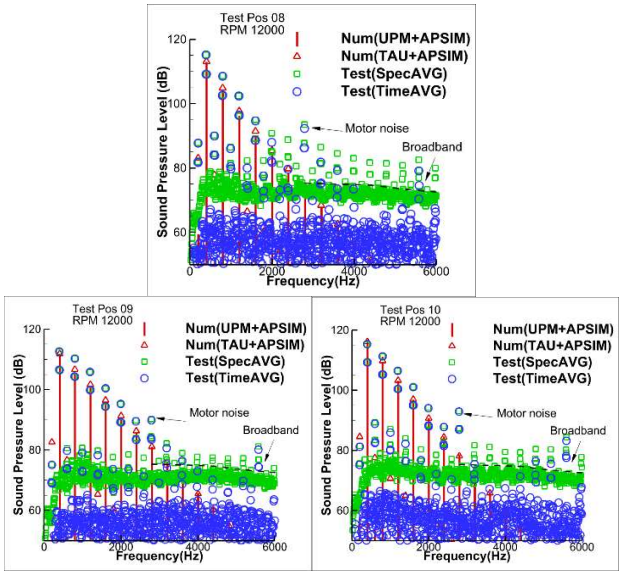

Figure 12 SPL spectra from microphones 8,9,10 for RPM 12000

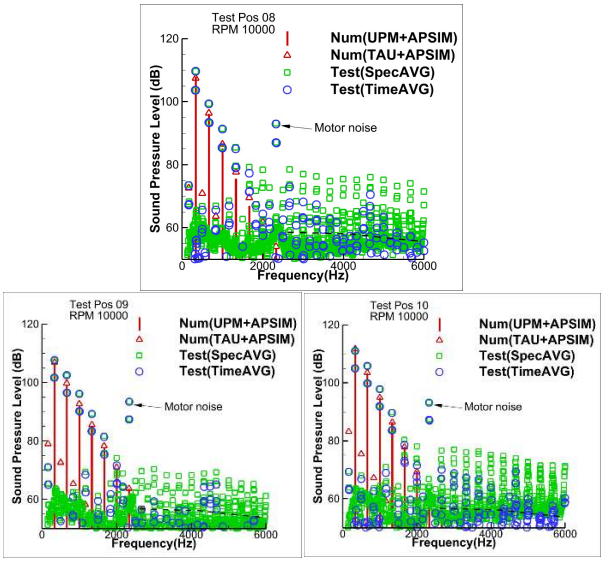

Figure 13 SPL spectra from microphones 8,9,10 for RPM 10000

The comparison of the spectrum indicates that:

1. For both the simulations and the test, the rotor harmonic sound components are found to dominate at low frequency. Broadband noise becomes more important for frequencies greater than 2 kHz;

2. The results using both UPM and TAU input match very well with each other in terms of amplitude of the harmonics and also the experimental trends. The highest level in the spectrum from the simulation is located at the first BPF and decays almost linearly with increasing frequencies; When comparing Figure

12 with Figure 13, the decay rate increases with decreasing RPM as a reduction in Mach number and hence in doppler amplification;

3. Subharmonics are observed in the TAU results and in the experiment. They are caused by the blade geometric asymmetry. In UPM two identical blades are assumed. The experimental results also show additional sub-harmonic contributions from the motor;

4. Broadband noise observed at the higher harmonics above 2000Hz is less important for the total noise;

5. In general motor noise contributes to all the rotor harmonics and its sub-harmonics, but the motor noise overwhelms the rotor contributions only at specific harmonics, especially for RPM 10000.

4.2 Forward flight at v=15m/s and RPM at 8000,10000,12000

For this study, the impact of the rotor RPM on the rotor performance and noise is studied. The rotor shaft angle is kept at 0°.

4.2.1 Trim conditions

The collective pitch correction to achieve test thrust is summarized in Table 2 for different RPM. The rotor thrust increases with increasing the rotor RPM. Similar to the hover condition, a decrease in the pitch angle is observed. In forward flight, more reduction on the pitch angle is required to match the test thrust, indicating a lesser induction from the wake on the rotor inflow, as the wake convects further downstream and away from the rotor.

Table 2 Trim conditions at shaft angle=0

V_∞ m/s	RPM	M_h	Pitch UPM	Thrust UPM	Thrust Test
15m/s	8000	0.41	-2.12	27.1	26.8
15m/s	10000	0.51	-2.47	40.0	40.0
15m/s	12000	0.61	-3.19	54.7	54.9

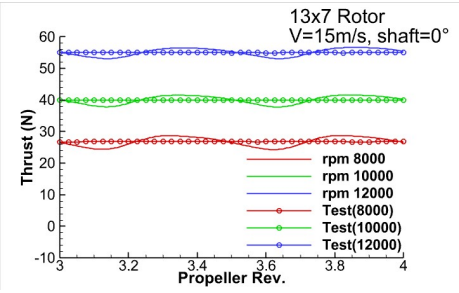

Figure 14 Rotor thrust as a function of rotor revolutions at different RPM

In forward flight, the blade local flow speed is a vector of the forward flight speed superimposed with the circumferential speed due to rotor rotation. This leads to a variation of the blade local on-flow. On the advancing blade side, the impact of the free stream increases the on-flow velocity and at the retreating side the on-flow velocity will be decreased. Therefore, due to the fixed blade pitch angle the blade force on the advancing blade side is increased and decreased on the retreating blade side. This causes a two-per-rev periodic force development in a sinusoidal variation as shown in Figure 14 for two bladed rotors.

4.2.2 Aerodynamics

Figure 15 plots the development of blade normal force coefficient C_NM^2 for different RPM. The one per revolution (1-P) behavior is clearly seen. It is expected that the lift variation in 1-P behavior will contribute to high harmonic loading noise.

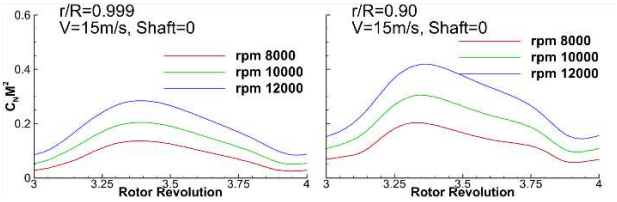

Figure 15 Time history of normal force coefficient C_NM^2 at two tip region sections

4.2.3 Acoustics

A comparison of the OASPL polar directivity is shown in Figure 16 for different rotor RPM. The dashed lines represent the noise obtained from time averaged test data while the solid lines denote simulation results. The trends with varying microphone position and increased RPM are captured. The numerical simulations in general underestimate the absolute value for all RPM in this flight condition, especially for the microphones below the rotor (mic. 5 to 9). A better correlation between simulations and test data is observed for the microphones above the rotational plane (mic.10 and 11).

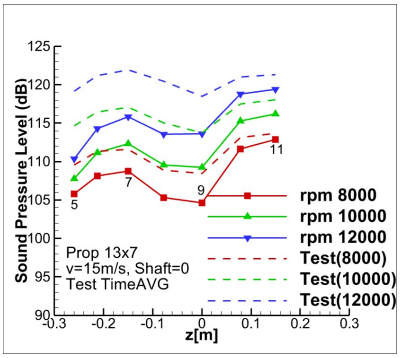

Figure 16 OASPL polar directivity at polar microphones from 5 to 11. Comparison of different RPM at forward flight

The comparison of the spectrum for RPM 12000, as shown in Figure 17, indicates that for both the simulations and the test, the rotor harmonic sound components are found to dominate at low frequency. The highest level in the spectrum from both the simulation and test is located at the first BPF and decays with increasing frequencies. Comparing with the hover as shown in Figure 12, the decay rate is relatively slow in the forward flight, as increasing the unsteady noise. There is increasing broadband noise or background flow noise in the test, but still remaining well below the rotor contribution [4]. Background flow noise is introduced due to the wind tunnel stream but also due to flow interaction with the in-flow microphone. This type of noise is not included in the simulations.

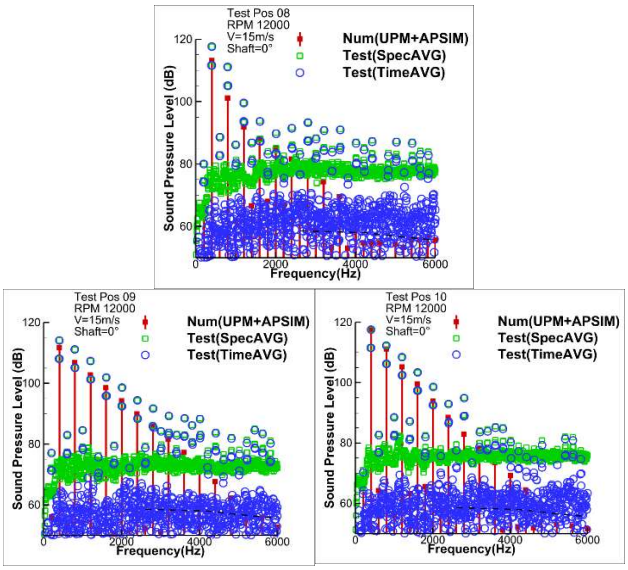

Figure 17 SPL spectra from microphones 8,9,10 for RPM 12000 at forward flight

5. RESULTS FOR TWO ROTORS IN COAXIAL CONFIGURATION

For the coaxial configuration, as shown in Figure 18, the coordinate system's origin lies at the middle point between each rotor in Z, centered on both axles in the X-Y plane. The distance between two rotors is defined by ΔZ/D, where D is the diameter of the rotor in 0.33m.

In the simulation, both rotors are identical (same geometry, same geometric pitch) and turn in opposite direction with the same rotational speed. The lower rotor defined as right-handed rotor (RHR) rotates count-clockwise as applied in isolated condition and the upper rotor defined as left-handed rotor (LHR) rotates then clockwise. The starting phase positions of the reference blade for both rotors point towards the downstream (Φ=0) and both rotors are phase locked. In the test however, there is no phase synchronization of the two rotors. Due to slightly different RPM of each rotor, the time averaged data may provide less relevant results. Therefore, only the spectrum averaged test data are used for the comparisons.

Some numerical results for two rotors with different starting position (Φ=45°,90°) will be given to show the effect of the phase delay between the rotors on the aerodynamic interaction and the acoustic interference.

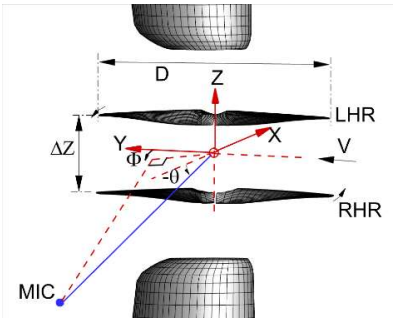

Figure 18 Coordinate and geometric definition for the coaxial rotor configurations (side view)

5.1 Hover at Δz/D=0.25 for rotor starting phase positions at Φ=0

5.1.1 Trim conditions

The collective pitch correction to match the test thrust is summarized in Table 3 for two RPM. The lower rotor (RHR) requires relative less pitch angle correction than the upper rotor (LHR) one to match the test thrust.

Table 3 Trim conditions

V_∞ m/s	RPM	M_h	Pitch UPM	Thrust UPM	Thrust Test
0	8000	0.41	RHR: -0.33° LHR: -1.17°	19.9N 23.7N	20.1N 23.8N
0	10000	0.51	RHR: -0.62° LHR: -1.14	30.8N 37.9N	31.2N 38.3N

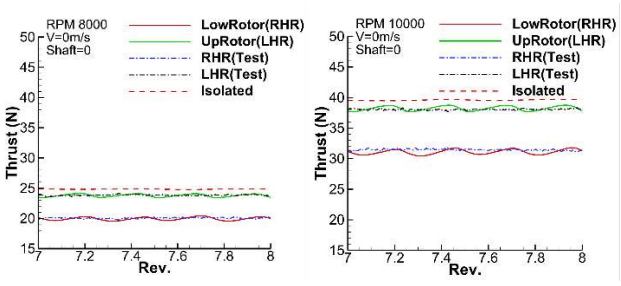

Figure 19 Rotor thrust as function of rotor revolution

The influence of the rotor-rotor interaction in hover condition can be demonstrated first by comparison with the isolated rotor thrust as shown in Figure 19. In coaxial configuration, there are two effects contributing to the interactions:

a. The multi-inductions of the wakes of both the upper rotor (LHR) and the lower rotor (RHR) cause deformations of the wakes and introduce additional downwash velocity. This reduces the effective angle of attack of both rotors, and therefore reduces the rotor thrust as shown in Figure 19 for both rotors when comparing to the isolated case. As RHR merges directly inside LHR wakes (Figure 20), this effect is much stronger for RHR and increases with increasing RPM. The influence is a function of rotor-to-rotor distance and RPM;

b. The rotor potential field (due to pressure) and displacement (due to blade thickness) causes additional multi-inductions among rotors and wakes. This effect introduces 4-per-rev variations with a maximum occurring at the blade position when LHR and RHR overlap.

5.1.2 Aerodynamics

A snap shot of the rotor wake development under influence of the rotor-rotor interactions is given in Figure 20 for RPM 8000. For clarity, only wake elements from one blade are shown. The lower rotor (RHR) and its wake merge with the wake of the upper rotor (LHR) and directly interact with the LHR wake. Interactions cause variation of the blade loads and the variations increase with increasing RPM, as shown in Figure 21, where the development of the normal force coefficient C_NM^2 is shown.

Figure 21 depicts the variation of C_NM^2 at two tip region sections and two RPM. All two radial stations show smooth variation of C_NM^2 values. The variation is slightly higher for RHR as it directly interacts with LHR wake. In general, the interaction is relative weak and smooth at these two sections.

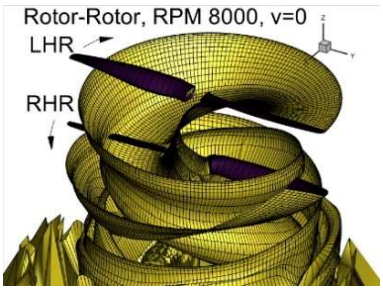

Figure 20 Snap shot of the rotor wake development under the influence of the rotor-rotor interactions

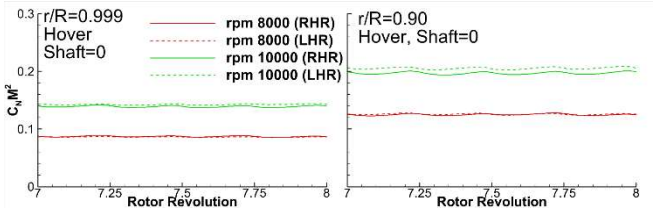

Figure 21 Time history of C_NM^2 at two tip region sections for coaxial rotors in hover

5.1.3 Acoustics

Selected acoustic simulation results obtained at two microphone positions (M1(Φ=90°,θ=0), M2(Φ=90°, θ=-30°)) in the X-Z plane are compared with the test results, as shown in Figure 22 and Figure 23 for two rotor RPM. The spectral-averaged test data are chosen to better emphasize the relative importance of both the broadband and tonal components of the source.

For the microphone located at M1, the low frequency BPF harmonics are the dominant source of noise and RHR noise is dominant contributor to the SPL. In the test results, there is a clear increase in tonal component levels from the 3rd BPF harmonics upward for RPM 8000 and from the 5th BPF harmonics upward for RPM 10000. The increase in higher harmonic tonal component levels in the test may indicate more interactions related unsteadiness or an effect of the unsynchronized speed in the experiment.

For the microphone located at M2, both RHR and LHR noise are equally important contributors for first 3 tonal components and two RPM. Comparing with M1, the level dropdown for low frequency harmonic value is much quicker, indicating less steady loading and thickness noise contribution to this microphone. An increase in higher harmonic tonal components is also observed. For lower harmonics the difference between the simulation and the experiment is relative larger than that for the microphone at M1, especially for first BPF. This can be caused by the coherent summation used by the sum of two rotor components in the simulations. The effect of the coherent sum of the signal can be demonstrated more clearly in the time histories as shown Figure 24 for RPM 8000 and 10000. For a reference, a time averaged test results are also included. Figure 24 shows clearly that the noises from the RHR and LHR are nearly identical and in-phase at this microphone position and the overall acoustic signal is almost doubled (solid red) in the peak region. Therefore, the coherent sum can increase OASPL in 6dB. It should be mentioned that the coherent sum is necessary for rotors which are phase synchronized, therefore sum of the acoustic signal in time domain is required. Due to slight asynchronization of RHR and LHR in the measurement, the time averaging result (solid green)

only match the peak level from a single rotor. The high frequency oscillations in the test result for RPM 10000 represent the contribution of the motor noise.

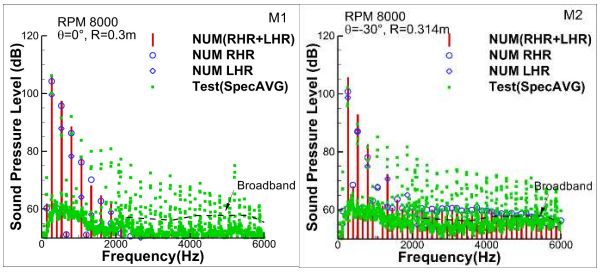

Figure 22 Sound pressure level (SPL) spectra from microphones Φ=90°, θ=0,-30° for RPM 8000

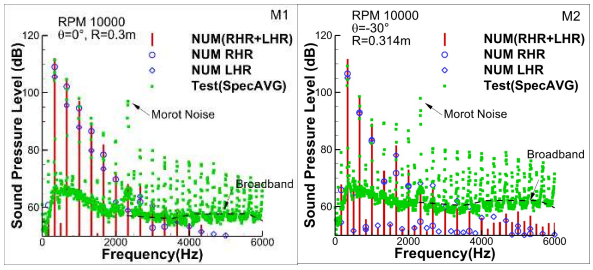

Figure 23 Sound pressure level (SPL) spectra from microphones Φ=90°, θ=0,-30° for RPM 10000

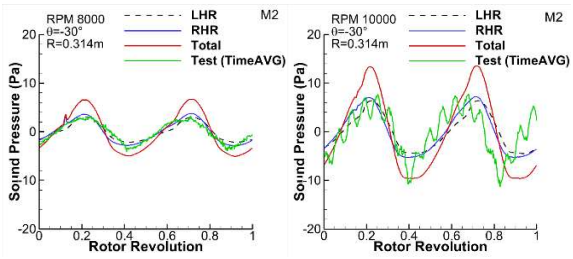

Figure 24 Sound pressure time histories for the RHR, LHR and a coherent sum of them

Acoustic assessments, represented in overall sound pressure level (OASPL) on a 150m hemisphere are show in Figure 25 and Figure 26 for two RPM. The hemisphere is centered at the coordinate origin (Figure 18) and underneath the rotors. For comparison, the noise from the isolated rotor as well as the noise from upper (LHR) and lower (RHR) rotor under interaction conditions are also given.

The noise directivity for RHR (low left) and LHR (top right) in the coaxial condition for both RPM bears strong similarity to the isolated one (low right). The noise emission shows an increment of the noise level when the microphone moves away from the rotor axis, which demonstrates the typic characteristics of the contribution from the steady loading noise. The contour pattern is slightly deviated from the symmetric one. The noise level around the rotor axis increases in the coaxial condition, indicating the contribution from the unsteady loading noise.

Moreover, with the coherent sum (RHR+LHR) in time domain), the interferences are particularly well visible in top left of Figure 25 and Figure 26. The contour pattern becomes more complex. The acoustic interference with acoustic signal cancelation (blue arrow) and enhancement (red arrow) are clearly seen.

In coaxial configuration, the maximum noise level for RHR and LHR deviated for both RPM from the isolated case by 0.1 and 0.3 dB, respectively. Compared to RHR or LHR, the maximum value for RHR+LHR increases about 5.8 and 5.9 dB, respectively, which corresponds to almost twice the sound pressure as indicated in Figure 24.

It should be mentioned that the coherent sum is necessary for rotors which are phase synchronized. Therefore, the sum of the acoustic signal in time domain is required. In order to show the influence of the acoustic interference using the coherent sum, the noise footprint with an incoherent sum of RHR+LHR is given in Figure 27 for two RPM. It is observed that in the incoherent sum the contour pattern deviates not significantly from RHR or LHR, as two rotors have similar noise directivity and no phase information from the acoustic signal is considered. Compared to the coherent sum, the maximum noise level is about 3dB lesser than that of the coherent sum. For this hover configuration, the rotors operating at an incoherent condition is better for less maximum noise level.

In a real situation the coherent level between the two rotors can be weaker than that for the full coherent case demonstrated here, because the asynchronization of the rotors, the noise scattering or reflection from other components may change the phase information of the signal.

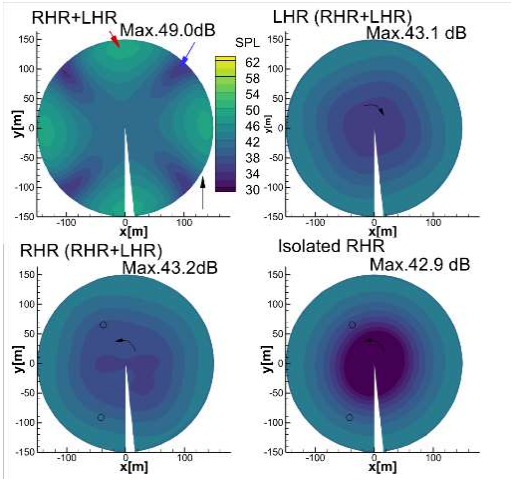

Figure 25 Noise contours in OASPL on 150m hemisphere underneath the rotors (RPM 8000)

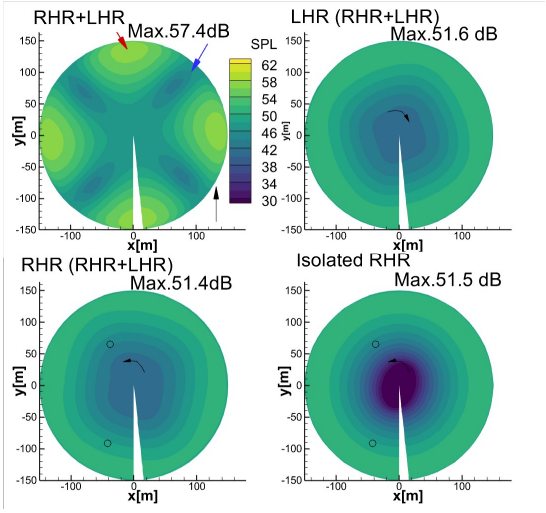

Figure 26 Noise contours in OASPL on 150m hemisphere underneath the rotors (RPM 10000)

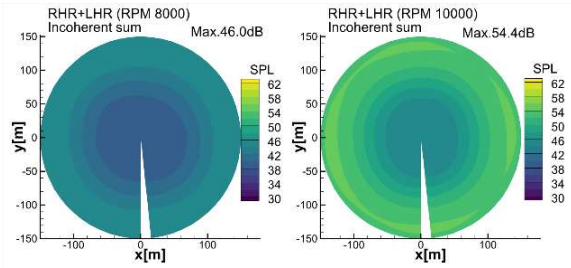

Figure 27 Noise contours in OASPL on 150m with an incoherent sum of RHR+LHR for RPM 8000, 10000

5.2 Hover at Δz/D=0.25 for two rotors with two starting phase positions (Φ_i = 45° and 90°)

In the previous section, the coherent sum shows strong acoustic interference effects. Therefore, two rotors with different starting phase position are simulated to show the effect of the phase delay between the rotors on the aerodynamic interaction and the acoustic interference.

The phase delay between the rotors are set at the rotor starting phase positions Φ_i = 45° and 90° respectively, as shown in Figure 28. The phase delay is only applied on the lower rotor RHR. The starting position of the upper rotor LHR is fixed at Φ_i = 0°.

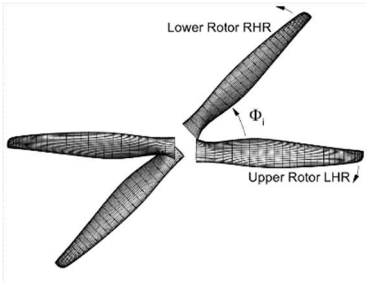

Figure 28 Coaxial rotors with different starting phase delay (top view)

5.2.1 Aerodynamics

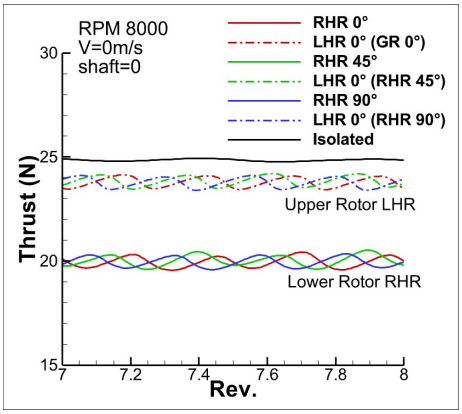

Figure 29 Rotor thrust as a function of rotor revolution for different phase delay

The trim conditions derived from Table 3 corresponding to Φ_i = 0° are applied. There is no change on the rotor thrust, indicating that the time averaged inflow is not changed. The effect of the phase delay shows that the influence of RHR phase angle mainly shifts the positions of interaction peaks due to change the relative positions among the blades, as shown in Figure 29.

5.2.2 Acoustics

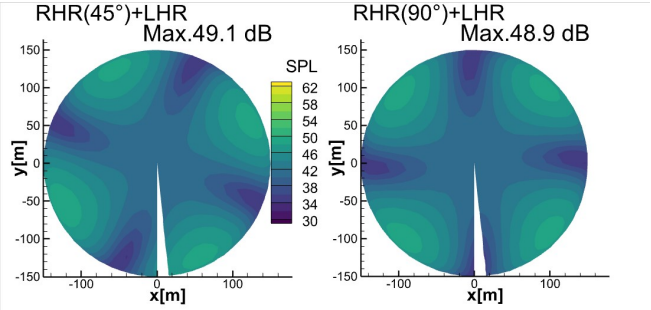

Figure 30 Total noise contour from the coherent sum (RHR+LHR in the time domain)

Compared with the results without the phase delay as shown in the top left contour of Figure 25, Figure 30 shows the change on maximum sound pressure level only within 0.1dB for both phase delays, except the rotation of the noise contour in an angle about the half of the phase delay. Therefore, the details of the potential fields, the interactions between the upper and lower rotor as well as the details of the wake-propeller interactions are not important for this configuration to define the maximum OASPL.

5.3 Forward flight at Δz/D=0.25 for rotor starting phase positions at Φ=0

5.3.1 Trim conditions

The collective pitch correction to achieve test thrust is summarized in Table 4.

Table 4 Trim conditions

V_∞ m/s	rpm	M_h	Pitch UPM	Thrust UPM	Thrust Test
15	8000	0.41	RHR: -1.46° LHR: -3.04°	22.7N 23.0N	22.7N 23.0N
15	10000	0.51	RHR: -1.91° LHR: -2.51°	32.4N 37.0N	32.0N 37.0N

In forward flight, more pitch correction is required in comparison with the hover condition. Similar characteristics of two-per revolution force development like in the isolated case remain for the coaxial configuration, as shown in Figure 31 for both RPM 8000 and RPM 10000. The multi-interaction causes the deviation of the two-per-revolution from a sinusoidal variation. For RPM 8000, there is only a very small difference in averaged thrust between RHR and LHR. For RPM 10000, the thrust difference between the two rotors increases. The form of time histories is similar to that of RPM 8000.

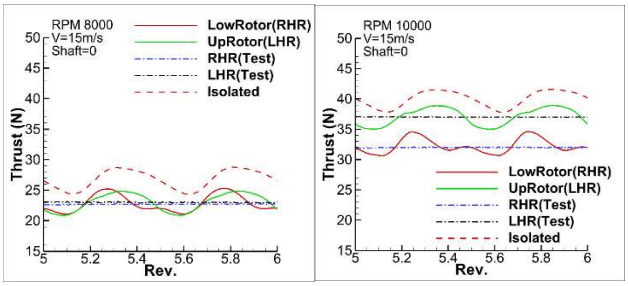

Figure 31 Rotor thrust as a function of rotor revolution at RPM 8000 and 10000

5.3.2 Aerodynamics

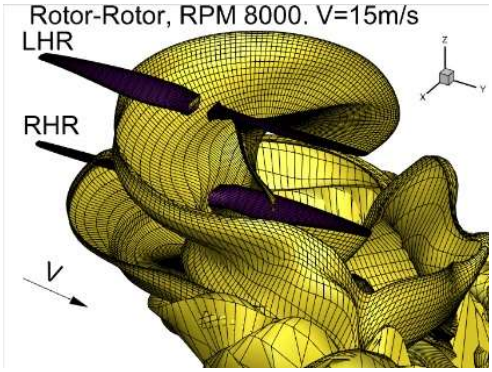

Figure 32 Snap shot of coaxial-rotor wake development in forward flight

A snap shot of the coaxial-rotor wake development in forward flight is given in Figure 32 for RPM 8000. Similar to the hover condition, the merging of the LHR and the RHR wakes as well as direct interactions of the RHR with the LHR wake can be seen. Due to additional convection speed from forward flight, the wakes move more quickly away from the rotor.

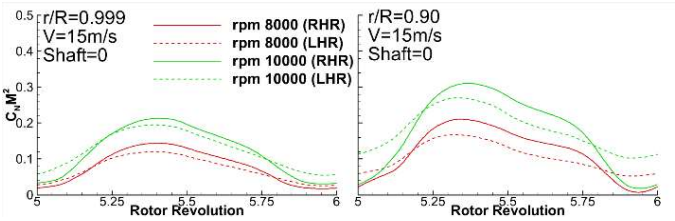

Figure 33 Time history of C_NM^2 at two tip regions for coaxial rotor at forward flight

Figure 33 plots the development of the normal force coefficient C_NM^2. Compared to the isolated case in Figure 15, multi-interactions have caused many changes especially for the RHR in the first and fourth quadrant, where the loads difference between the two RPM are reduced. This indicates closer rotor-wake interactions.

5.3.3 Acoustics

The acoustic spectra obtained at two microphone positions (M1(Φ=90°,θ=0), M2(Φ=90°, θ=-30°)) are compared with the test results for RPM 8000 and 10000 in Figure 34 and Figure 35. Both M1 and M2 are located in the X-Z plane, where M1 is also in the X-Y plane.

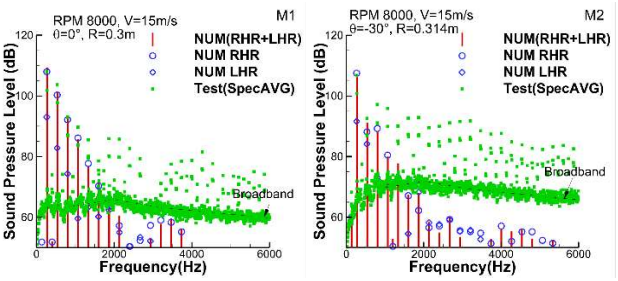

Figure 34 SPL spectra at two microphone positions in the X-Z plane for RPM 8000

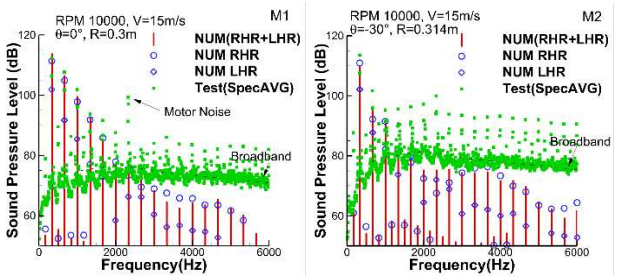

Figure 35 SPL spectra at two microphone positions in the X-Z plane for RPM 10000

For the microphone M1, both numerical and experimental results show that the rotor harmonic

noise till 3rd to 4th BPF from the RHR is the dominant source of noise for both RPM. The numerical and test results compare relative well in several low frequency tonal components and deviate with each other for the higher harmonics, indicating more unsteadiness in the test.

For the microphone M2, numerical results in general underestimate the higher harmonics of the test results. Similar to M1, there is a clear increase in tonal component levels from the 3rd BPF harmonics upward in the test. The broadband noise is significantly stronger compared with the M1 position. M2 is located in the plane below the rotational plane of the two rotors and may encounter the downwash flow from both rotors. Therefore, high broadband noise can partly be attributed to the microphone self-noise.

It has to be mentioned that in the numerical simulation the pylon wake is ignored and the influence of the pylon wake can be an additional reason for the differences.

A comparison of the noise contour directivity for the overall sound pressure level is shown in Figure 36 and Figure 37 for RPM 8000 and 10000, respectively. The noise directivity is characterized by the dominant loading noise for LHR, RHR and RHR isolated. The acoustic interferences in RHR+LHR are well visible and shift the area of the maximum noise further downstream. The maximum noise level increases about 0.9 dB for the lower rotor (RHR) for both RPM, while 0.4dB less noisy is observed for the LHR for RPM 8000. Compared to RHR or LHR, the coherent sum of both rotors increases the maximum noise level about 4.8 and 6.1 dB, respectively, which is similar to the analysis in the hover condition.

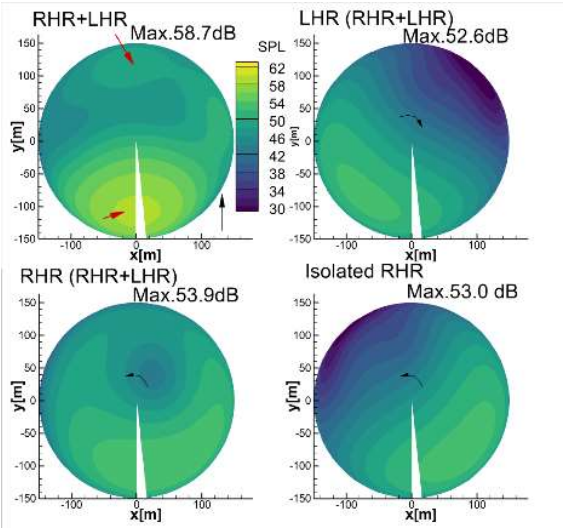

Figure 36 Noise contours in OASPL on 150m hemisphere underneath the rotors (RPM 8000)

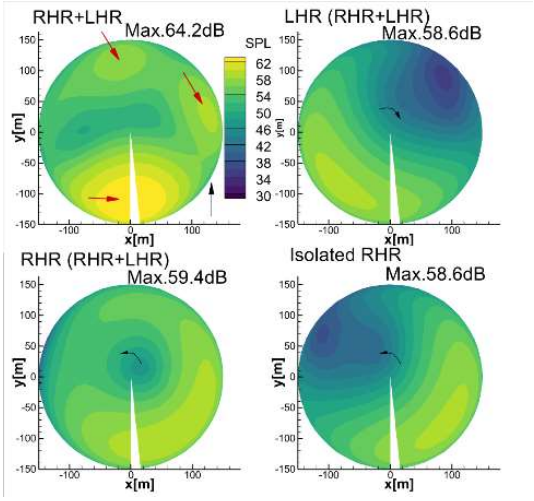

Figure 37 Noise contours in OASPL on 150m hemisphere underneath the rotors (RPM 10000)

5.4 Forward flight at Δz/D=0.25 for two rotors with two starting phase positions (Φ_i = 45° and 90°)

Two rotors turning at RPM 8000 with different starting positions are simulated. The phase delay between the rotors are set at 45° and 90° respectively. The phase delay is only applied on the lower rotor RHR, as shown in Figure 28. The starting position of the upper rotor LHR is fixed at Φ_i = 0° and points to the downstream.

5.4.1 Aerodynamics

The trim conditions derived from Table 4 is applied. There is no additional correction on the blade pitch angel required. Therefore, the time averaged inflow is not changed by the phase angles. Compared with the results without the phase delay as shown in Figure 38 for RPM 8000 in solid line, the effect of the phase delay changes not only the positions of maximum peaks, but also changes both the form and the amplitude of the curve. There is a slight increase in the amplitude when applying the phase angle.

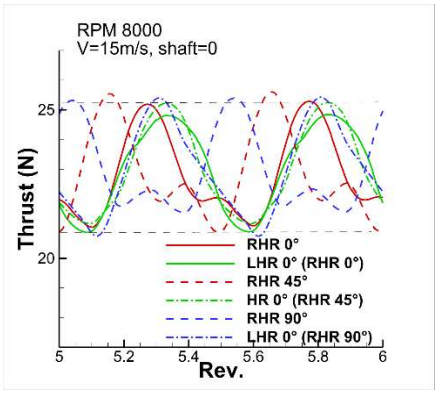

Figure 38 Rotor thrust as function of rotor revolution for different phase delay

5.4.2 Acoustics

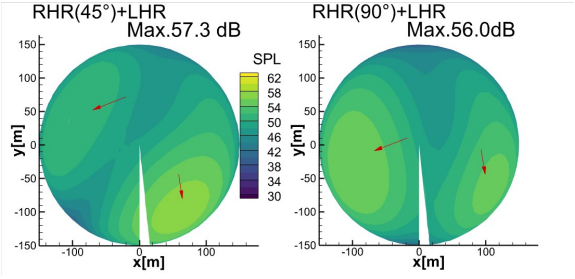

Figure 39 OASPL contour from the coherent sum of the RHR+LHR for RPM 8000

OASPL contours for the two-phase angles are given in Figure 39 for RPM 8000. Compared with the results without the phase angle as shown in Figure 36 top left, the change of both the noise directivity and the maximum noise level are observed. Due to the change of the signal phase angle introduced by the blade phase delay, the interference peaks pointed by red arrows are rotated count clockwise. The maximum level reduces about 1.4 dB for 45° and 2.7 dB for 90° respectively.

6. RESULTS FOR TWO ROTORS IN TWO TANDEM CONDITIONS

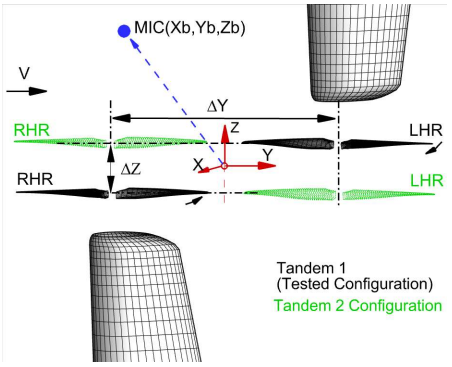

Figure 40 Coordinate and geometric definition for the tandem rotor configurations

For the tandem configuration, both rotors are in a plane which is parallel to the y-x plane. The origin of the coordinate system lies at the mid-point between both rotor axles. Both rotors turn in opposite direction with the same rotational speed. The upstream rotor defined as right-handed rotor (RHR) rotates count-clockwise and the downstream rotor defined as left-handed rotor (LHR) rotates clockwise. Results for the tandem configurations with ΔY= 1.18D and ΔZ = +/- 0.25D are studied:

1. Tandem 1: the downstream rotor located above the upstream rotor, ΔZ = 0.25D, as shown in black in Figure 40;
2. Tandem 2: the downstream rotor located below the upstream rotor, ΔZ = 0.25D, as shown in green in Figure 40. As no test conducted, the thrust from tandem 1 is used.

6.1 Forward flight for two rotors with same starting position

6.1.1 Trim conditions

The collective pitch correction to achieve test thrust is summarized in Table 5.

Table 5 Trim conditions (V_∞ =15 m/s)

Tandem	RPM	M_h	Pitch UPM	Thrust UPM	Thrust Test
1	8000	0.41	RHR: -2.51 LHR: 0.83	26.4 24.7	26.3 25.0
2	8000	0.41	RHR: -2.42 LHR: -1.53	26.3 24.5	26.3 25.0

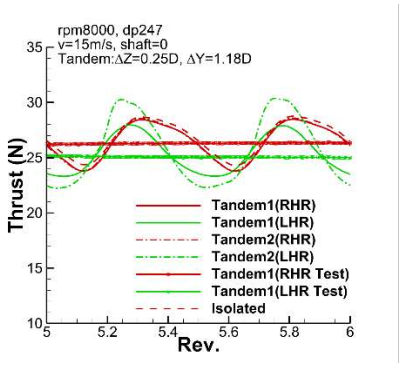

Figure 41 Rotor thrust as function of rotor revolutions in 2 tandem configurations

The multi-interaction causes a deviation of the two-per-revolution form noticed for the isolated case. The form of the LHR thrust in one rotor revolution deviates strongly from the form of the RHR. This indicates that the influence of the RHR/LHR multi-induction has a much stronger effect on the LHR, especially for the tandem 2 configuration. The thrust form of the upstream rotor (RHR) is less affected by the interactions, which has very similar form and amplitude like isolated one.

6.1.2 Aerodynamics

Two snap shots of the rotor wake development for the two tandem configurations are shown in Figure 42. For the tandem 1 configuration, the wakes from upstream rotor (RHR) convect down stream and pass underneath the downstream rotor (LHR). In the far-field both rotor wakes merge. For the tandem 2 configuration, the RHR wakes pass very colse to and

partly through the LHR and its wakes. The rolled-up wing tip like wakes of the RHR hit the LHR and deform the LHR wake strongly. The strong induction of the RHR wake distorts and absorbs the LHR wake. The direct interactions of the RHR wakes can cause strong variation in the rotor aerodynamic, as shown in Figure 41.

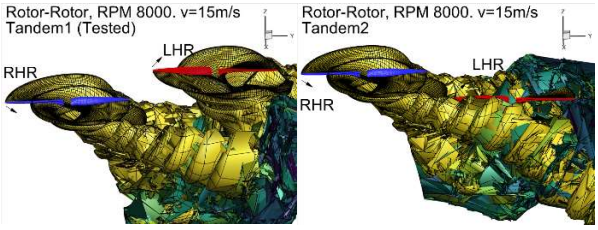

Figure 42 Snap shot of the rotor wake development in the tandem configurations, top: tandem 1, bottom: tandem 2.

6.1.3 Acoustics

The acoustic spectrums obtained at three microphone positions in the X-Y plane for the Tandem 1 configuration are compared with the test results in Figure 43. Three microphones are located at the upstream of RHR (M1), and up (M2)- and downstream (M3) of LHR, respectively.

For M1, the first 4 low frequency BPF harmonics are the dominant source of noise. For these 4 BPFs, the RHR noise is the dominant contributor to the noise level. At first BPF, the contribution of the LHR reduces slightly the overall noise. This indicates that the acoustic signal from the RHR and the LHR is slightly out of phase and some cancelation of two signal occurs for this microphone. In the test results, there is a clear increase in tonal component levels from the 5th BPF harmonics upward, but their contributions to the OASPL can be neglected.

For M2, the noise from both the RHR and the LHR is equally important for first two BPFs. Therefore, the influence of the acoustic interference effect between the rotors can be stronger than M1. The summation of the RHR and the LHR, enhances the noise level till 3rd BPF. This indicates that the acoustic signal from the RHR and the LHR is in-phase. Compared with M1, the level dropdown with increasing the frequency is much quick, indicating less steady loading noise contribution.

For M3, there is increasing broadband noise or background flow noise in the test, as the M3 is located at the downstream of the two rotors. At this position, the microphone may already be located in the induced flow area where the axis of the microphone may largely deviate from the flow stream line. This increases the background noise due to the flow interaction with the in-flow microphone.

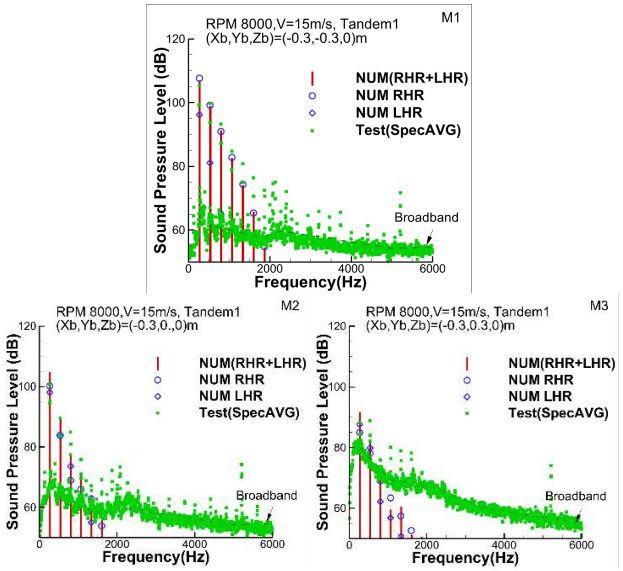

Figure 43 SPL spectra from the microphone located at M1 to M3

A comparison of the noise contour directivity for the two tandem configurations is shown in Figure 44. The noise directivity for both configurations bears strong similarity. The noise emission shows an increment of the noise level for tandem 2 due to higher the interaction noise for the downstream rotor. The maximum noise level for tandem 2 increases about 2 dB.

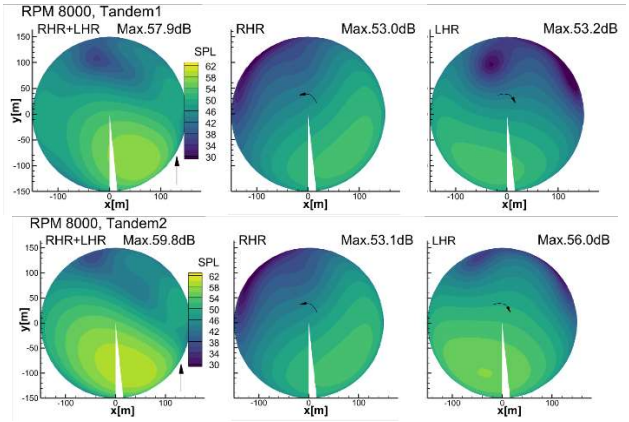

Figure 44 Noise contours directivity on 150m hemisphere for two tandem configurations

CONCLUDING REMARKS

The acoustic and aerodynamic characteristics of small-scale multi-rotor configurations for various flight conditions are simulated and compared with available test data. An unsteady free wake panel code was used to account for the influence of the rotor-rotor interactions. The acoustic characteristics were calculated with a FW-H code. The results indicated

that the noise emission of the rotors can be significantly affected by multi-interactions. The experiments and numerical results indicate that the harmonic noise is the dominant source of the noise for the rotors studied. Broadband noise is observed in the test, but the contribution to the overall sound pressure is small. In the coaxial configuration the acoustic interferences are particularly well visible in the numerical simulation. The interference can increase or decrease the maximum noise level. The study of the phase delay between the rotors indicated that in the forward flight, the phase delay can be used to reduce the noise radiation. The study of the tandem configuration showed that the position of the downstream rotor is key for the noise radiation and therefore avoiding the interaction with upstream wake can reduce the noise radiation.

REFERENCES

[1] A. Straubinger, R. Rothfeld, M. Shamiyeh, K.-D. Büchter, J. Kaiser und K. O. Plötner, „An overview of current research and developments in urban air mobility – Setting the scene for UAM introduction“, Journal of Air Transport Management, Bd. 87, Nr. -, p. 101852, 2020.

[2] W. Johnson und C. Silva, „NASA concept vehicles and the engineering of advanced air mobility aircraft“, The Aeronautical Journal, Bd. 126, Nr. 1295, pp. 59-91, 2022.

[3] M. Pott-Pollenske, J. W. Delfs, “Enhanced Capabilities of the Aeroacoustic Wind Tunnel Braunschweig”, 14th AIAA/CEAS Aeroacoustics Conference (29th AIAA Aeroacoustics Conference), 2008, AIAA-2008-2910.

[4] K.-S. Rossignol, J. Yin und L. Rottmann, “Investigation of Small-Scale Rotor Aeroacoustic in DLR's Acoustic Wind Tunnel Braunschweig”, in 28th AIAA/CEAS Aeroacoustics 2022 Conference., Southampton, UK, 2022.

[5] J. Yin “Prediction - and its Validation - of the Acoustics of Multiblade Rotors in Forward Flight Utilising Pressure Data from a 3-D Free Wake Unsteady Panel Method”. Proceedings, 20th European Rotorcraft Forum, 04. - 07.10.1994 in Amsterdam/Niederlande.

[6] S.R. Ahmed, V.T. Vidjaja, “Unsteady Panel Method Calculation of Pressure Distribution on BO105 Model Rotor Blades“, Journal of the American Helicopter Society, pp. 47-56, Jan. 1998.

[7] J. Yin, S.R. Ahmed, “Helicopter main-rotor/tail-rotor interaction”. Journal of the American Helicopter Society, Vol. 45 (No. 4), pp. 293 -302, 2000.

[8] J. Yin, B.G. van der Wall, G.A. Wilke “Rotor Aerodynamic and Noise under Influence of Elastic Blade Motion and Different Fuselage Modeling”. 40th European Rotorcraft Forum (ERF) 2014, 2-5 September 2014, Southampton, UK.

[9] P. Kunze, “Approximate Boundary Layer Methods for a Fast Mid-Fidelity Aerodynamics Code for Helicopter Simulations”. Springer Nature Switzerland. New Results in Numerical and Experimental Fluid Mechanics XIII, Virtuell. doi: 10.1007/978-3-030-79561-0_36. ISBN 978-3-030-79560-3. ISSN 1612-2909, 2021

[10] M. Tugnoli, D. Montagnani, M. Syal, G. Droandi A. Zanotti, “Mid-fidelity approach to aerodynamic simulations of unconventional VTOL aircraft configurations”. Aerospace Science and Technology 115, 2021

[11] D. Schwarmborn, T. Gerhold, R. Heinrich, “The DLR TAU-Code: Recent Applications in Research and Industry”, Proceedings of European Conference on Computational Fluid Dynamics ECCOMAS CFD 2006, Delft, Netherlands.

COPYRIGHT STATEMENT